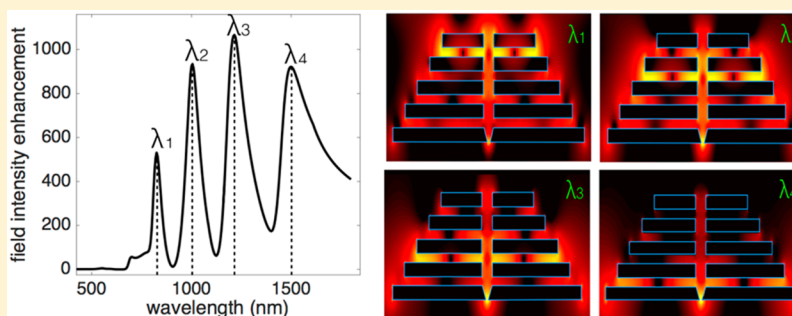


# Plasmonic Circuit Theory for Multiresonant Light Funneling to a Single Spatial Hot Spot

Tyler W. Hughes<sup>†</sup> and Shanhui Fan<sup>\*,‡</sup>

<sup>†</sup>Department of Applied Physics and <sup>‡</sup>Department of Electrical Engineering, Stanford University, Stanford, California 94305, United States



**ABSTRACT:** We present a theoretical framework, based on plasmonic circuit models, for generating a multiresonant field intensity enhancement spectrum at a single “hot spot” in a plasmonic device. We introduce a circuit model, consisting of an array of coupled LC resonators, that directs current asymmetrically in the array, and we show that this circuit can funnel energy efficiently from each resonance to a single element. We implement the circuit model in a plasmonic nanostructure consisting of a series of metal bars of differing length, with nearest neighbor metal bars strongly coupled electromagnetically through air gaps. The resulting nanostructure resonantly traps different wavelengths of incident light in separate gap regions, yet it funnels the energy of different resonances to a common location, which is consistent with our circuit model. Our work is important for a number of applications of plasmonic nanoantennas in spectroscopy, such as in single-molecule fluorescence spectroscopy or Raman spectroscopy.

**KEYWORDS:** Plasmonics, nanoantenna, circuit model, field intensity enhancement, multiple resonances, hot spot

Metallic nanostructures are of great current interest due to their ability to achieve large, localized enhancements for incident light.<sup>1–3</sup> In many applications, moreover, it is desirable to develop the capability to funnel multiple wavelengths resonantly into a single spatial hot spot. In single-molecule fluorescence experiments, for example, one would like to simultaneously enhance the fields at the molecule location for both the excitation and the emission wavelengths.<sup>4,5</sup> Such a capability may also be useful in Raman spectroscopy. By using a nanostructure to generate field enhancement at the incident wavelength as well as multiple Raman scattering wavelengths, one may obtain molecule-specific spectral fingerprint information from surface-enhanced Raman spectroscopy (SERS).<sup>6,7</sup> Therefore, for these applications, it would be useful to have a general theoretical framework for designing structures that are able to generate field enhancement at a single hot spot for multiple resonance wavelengths.<sup>8–10</sup>

A simple antenna, such as an optical dipole antenna, typically supports only one dominant resonance over a fairly broad range of wavelengths.<sup>11,12</sup> One could, of course, create a multiresonant antenna by placing several of these dipole antennas together, each with a slightly different length and, hence, a different resonance frequency. However, there is no guarantee that this combined antenna can funnel multiple resonance

wavelengths to the same spatial hot spot. Many works have utilized complicated metal geometries with a probe tip, such as bowties,<sup>13,14</sup> fractal geometries,<sup>15–18</sup> and jagged edged structures,<sup>19–21</sup> to add resonances to the spectrum of the dipole antenna. However, these additional resonances often do not lead to substantial field enhancement at a common location because their geometric features do not efficiently induce charge buildup at the probe tip for each resonance. Additionally, these devices do not always display predictive control over what specific resonance wavelengths are excited because complicating the structure geometry makes methodical tuning less straightforward.

In this Letter, we develop a circuit theory that can be used to guide the design of a metallic nanoantenna for multiresonant field enhancement at a single hot spot. The circuit under investigation consists of a series of LC resonators, and we show that the relative position of these resonators in the circuit are essential to funneling energy to a single element for multiple resonance frequencies. Using plasmonic equivalent circuit models, we realize the theory in a physical system as shown

**Received:** June 17, 2016

**Revised:** August 9, 2016

**Published:** August 12, 2016

in Figure 1. The structure consists of five pairs of metallic rectangles. The important features of the structure are that the

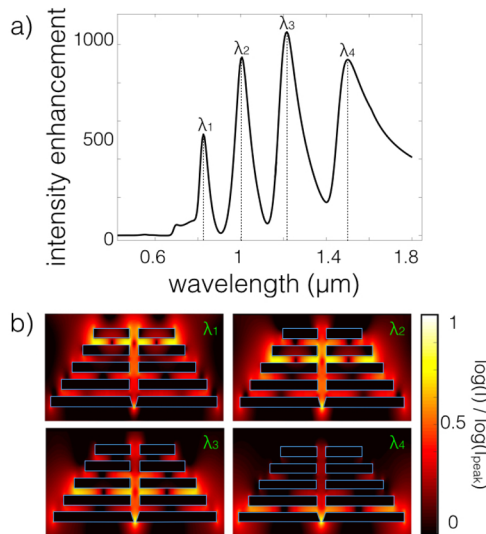


**Figure 1.** Simulation results for a metallic nanoantenna designed to achieve multiresonant funneling of light onto a single hot spot. Outlines of the structure are depicted in (b). Regions surrounded by blue are modeled as gold, with optical constants taken from tabulated data,<sup>22</sup> and the other regions are vacuum. In these simulations, the gold bar lengths are varied from 100 to 180 nm in increments of 20 nm. The thicknesses of the gold bars and the vacuum gaps are 20 and 15 nm, respectively. The spacing between the two halves of the device is 20 nm. The hot spot is located between the two longest metal bars. (a) Electric field intensity enhancement factor at the “hot spot” as a function of incident wavelength. Four resonance peaks are observed. (b) The logarithm of the intensity enhancement at each of the four resonance wavelengths shown in the spectrum in (a) normalized by the logarithm of the peak intensity on resonance. Each resonance is located in a gap region between the pairs of metal bars. While most resonances have fields that are concentrated away from the hot spot, the resonant energy is nevertheless funneled to the hot spot at all four wavelengths.

rectangles with the longest length are located at one end of the structure, and the length of the rectangles decreases away from this end. We attach a pair of probe tips between the metallic rectangles that have the longest length. A plane wave is normally incident from the top of the structure, with polarization in the horizontal direction. In Figure 1a, we measure the electric field intensity enhancement at a single location halfway between the sharp tips on the bottom of the structure as a function of incident wavelength and normalize this by the intensity of the incident wave.

$$I(\lambda) = \frac{|E_{\text{probe}}(\lambda)|^2}{|E_0(\lambda)|^2}$$

The spectrum consists of four peaks of comparable strength. Each of the resonant peaks in the spectrum correspond to a resonance located in a gap region between metallic regions, as shown in Figure 1b, where we plot the logarithm of the field intensity inside the structure when illuminated with a plane wave with frequency corresponding to that of each resonance peak of the spectrum. Even though most of these resonances have amplitudes that are located in a gap region away from the tip, the structure nevertheless enables the funneling of the resonant energy into the tip, resulting in a multiresonant field

enhancement at the single spatial hot spot between the probe tips, which is consistent with our circuit theory prediction.

To illustrate the concept, we begin by considering a simple circuit consisting of an array of LRC resonators as shown in Figure 2. A single LRC circuit has a resonance frequency given

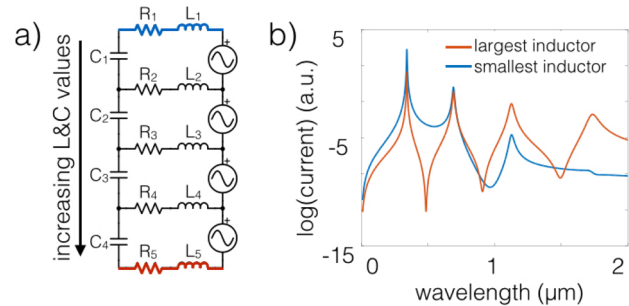


**Figure 2.** (a) Circuit model used to demonstrate multiresonant energy funneling to a single element. The circuit consists of a series of LRC resonators with  $L$ ,  $R$ , and  $C$  values cascaded from lowest to highest from top to bottom, respectively. (b) Absolute value of the current in the smallest (blue) and largest (red) inductor as a function of driving wavelength (log scale). A total of four resonance peaks are observed for this circuit containing four capacitor elements, as expected. All resonance peaks have comparable strength on the largest inductor (red), whereas on the smallest inductor (blue), the long-wavelength resonances are suppressed.

by  $\omega_0 = (LC)^{-1/2}$ , where  $L$  and  $C$  are the inductance and capacitance. In addition, the circuit contains a resistor to introduce loss. We seek to investigate how stacking resonators with different frequencies allows us to engineer energy transfer through the system. To do this, we use a configuration, as shown in Figure 2a, which consists of four capacitors. The parameters for these circuit elements, as exhibited in the Table 1, are chosen to

**Table 1. Circuit Parameters Used in Figure 2**

no.	$C$ ( $10^{-18}$ F)	$L$ ( $10^{-14}$ H)	$R$ ( $\Omega$ )
1	2.36	1.205	0.6061
2	4.13	2.109	1.0606
3	5.9	3.012	1.5152
4	7.67	3.916	1.9697
5		4.820	2.4242

approximately correspond what is appropriate for our antenna structures to be discussed later. We choose the  $L$ ,  $C$ , and  $R$  values to vary from low to high along the array, which results in the same variation of the resonance frequency along the array that we observe in Figure 1.

We place AC voltage sources directly over each of the LRC cells to drive the circuit and plot in Figure 2b the spectra of currents through the two inductors at the outer edges of the circuit. To facilitate comparison to optical simulations, here the spectra are plotted as a function of free-space wavelengths. Because the circuit consists of four LC resonators, as expected, we observe four resonance peaks in both spectra; however, there is noticeable difference in the peak amplitudes. Specifically, at the smallest inductor near the highest-frequency resonator location (blue), we notice that the intensity of the resonance peaks is greatly diminished as the wavelength is increased. Conversely, at the largest inductor near the lowest frequency resonator (red), the resonant peaks have more-

comparable strength. Therefore, while different resonances arise from different inductors and capacitors inside the circuit, all of these resonances efficiently funnel their current to the circuit elements near the resonators with the lowest frequency.

To explain the difference in the two spectra in Figure 2b, we focus on how the energy is transferred through a single LRC stage in the circuit shown in Figure 2a. When this single stage, as shown in Figure 3a, is driven by a harmonic input voltage of the form  $V_0 e^{j\omega t}$ , the transmitted voltage has the form  $V_1 e^{j\omega t}$ , where

$$V_1(\omega) = \frac{j\omega RC - \omega^2 LC}{1 + j\omega RC - \omega^2 LC} V_0(\omega)$$

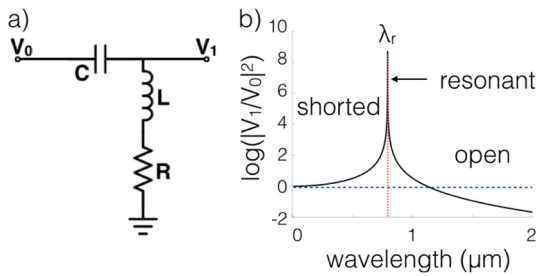


**Figure 3.** (a) Simple circuit representing one stage in the array in Figure 2a.  $V_0$  is the excitation voltage, and  $V_1$  is the transmitted voltage. (b) Transmission efficiency  $|V_1|^2/|V_0|^2$  for  $L = L_3$ ,  $C = C_3$ , and  $R = R_3$ . The blue dotted line represents  $V_1 = V_0$ . For wavelengths shorter than  $\lambda_r = 2\pi c_0 \sqrt{LC} = 794$  nm (where resonant wavelength is  $\lambda_r$ ), the circuit is shorted, and current can flow. Conversely, at wavelengths far above  $\lambda_r$ , the circuit is open and energy is not able to efficiently flow through this element.

As an illustration, in Figure 3b, we plot the transmission efficiency  $\left| \frac{V_1}{V_0} \right|^2$  as a function of frequency for  $L$ ,  $R$ , and  $C$  values corresponding to the third stage in the resonator array in Figure 2a (refer to Table 1 for values). Such a single stage behaves as a high-pass filter, i.e., a filter that allows high-frequency components of an excitation to transmit through while rejecting low-frequency components. The transmission efficiency has a resonance at a wavelength of 794 nm. For any wavelength below this resonant wavelength,  $\left| \frac{V_1}{V_0} \right|^2 > 1$  indicating that this circuit is electrically shorted and the current can flow through it. Conversely, above the resonance wavelength,  $\left| \frac{V_1}{V_0} \right|^2 < 1$  the circuit becomes electrically open and current does not flow through. Therefore, in the circuit of Figure 2a, when any individual resonator is on resonance, its energy, having a resonant wavelength  $\lambda_r$ , can be funneled effectively to the largest inductor at one end of the circuit because all the stages in between have resonant wavelengths larger than  $\lambda_r$  and are all electrically shorted. Conversely, the path between such a resonator and the smallest inductor located at the other end of the circuit is electrically open at the resonant wavelength  $\lambda_r$ . Therefore, the resonant energy at  $\lambda_r$  cannot effectively funnel to the smallest inductor. The high-pass filter behavior of the single circuit stage in Figure 3 therefore underlies the difference in current spectra for the two inductors located at the two edges of the circuit in Figure 2.

From the circuit model, we therefore have shown that to achieve multiresonant funneling of energy to a single location, we can use the circuit shown in Figure 2a, where we cascade a series of LC resonators with resonance frequencies varying from high to low. In this circuit, the lowest-frequency resonator will then exhibit strong resonant response at all of the resonance frequencies in the system, enabling multifrequency funneling to this single, lowest frequency resonator component.

We now translate the circuit model presented above into to a physical structure that is capable of multiresonant light funneling to a single spatial location. To do this, we make use of the previous work on equivalent circuit models for plasmonics<sup>23–28</sup> to design the basic working unit of a metallic nanostructure. The inductors and resistors in Figure 2a can be implemented using metal wires, which we describe by the Drude model for simplicity. Following the derivation presented by Staffaroni et al.,<sup>29</sup> at a frequency  $\omega$ , metal, with permittivity of  $\epsilon_m$ , has an optical conductivity,  $\sigma(\omega)$ , given by

$$\sigma(\omega) = j\omega\epsilon_0(\epsilon_m(\omega) - 1)$$

Thus, the impedance of a metallic wire of length  $l$  and cross-sectional area  $A$  is

$$Z_{\text{wire}} = \frac{1}{\sigma(\omega)} \frac{l}{A}$$

In the Drude model,  $\epsilon_m(\omega) = 1 - \left( \frac{\omega_p^2}{\omega^2 - j\gamma\omega} \right)$ , where  $\omega_p$  is the plasma frequency of the metal and  $\gamma$  is the damping rate, thus making the impedance:

$$Z_{\text{wire}} = j\omega \frac{1}{\epsilon_0\omega_p^2} \frac{l}{A} + \frac{\gamma}{\epsilon_0\omega_p^2} \frac{l}{A} = j\omega L + R$$

Therefore, we readily identify our circuit elements in terms of physical parameters as  $L = \frac{1}{\epsilon_0\omega_p^2} \frac{l}{A}$  and  $R = \frac{\gamma}{\epsilon_0\omega_p^2} \frac{l}{A}$ . The capacitors from our circuit model are implemented as capacitive coupling between these metal bars. The capacitance between metal bars of length  $l_i$  and  $l_j$ , with a height  $h$  and gap space  $w$ , is approximately:

$$C \approx \min(l_i, l_j) \frac{h}{w} \frac{1}{\epsilon_0}$$

Thus, we can use the values derived above to implement a single LRC circuit resonator as a metal–insulator–metal (MIM) structure, as shown in Figure 4a. To implement the

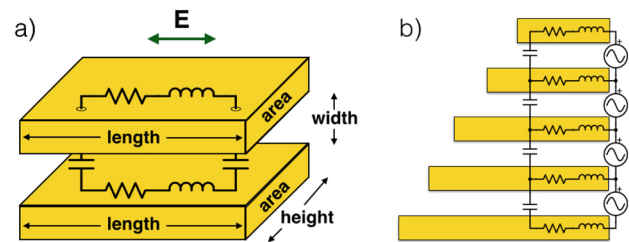


**Figure 4.** (a) Physical implementation of an LRC resonator. Here, we use metal bars to serve as inductive and resistive elements and bring them together to introduce capacitance. (b) Stacking these unit cells together with metal bars of different lengths allows us to implement our original circuit from Figure 2 and produces a basic version of the nanostructure that we introduce in this work.

array of LRC resonators that we introduced above, we simply stack these resonators together with decreasing metal bar lengths, resulting in the metallic nanostructure depicted in Figure 4b. The driving source in Figure 2a, previously modeled as AC voltage sources, can now be implemented by illuminating this structure with monochromatic light. Finally, instead of measuring current through the inductors, in the simulation we measure the field enhancement at the edges of the metal bars.

We simulate a 2D version of the structure in Figure 4b using finite-difference frequency domain (FDFD) electromagnetic simulations,<sup>30,31</sup> as shown in Figure 5. In the simulation, we

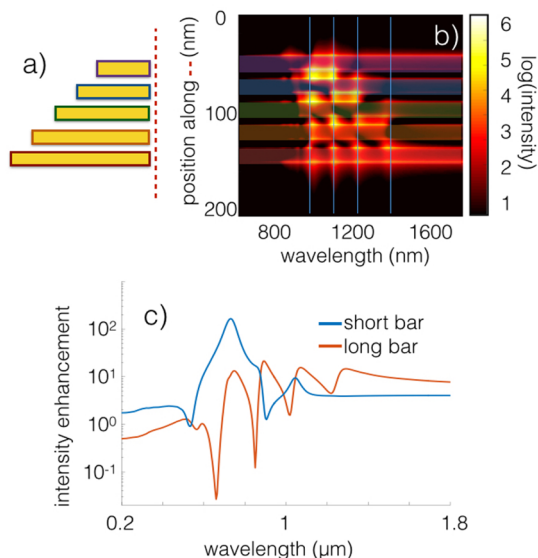


**Figure 5.** Electromagnetic validation of circuit model from Figure 2. (a) Simulated geometry. The yellow regions represent the metal bars. The regions between the metal bars are air. Geometric and material parameters used here are the same as those described in Figure 1. (b) Field-intensity enhancement along the red dotted line in (a) as a function of wavelength (log scale). We notice that all four resonance peaks are evident in the vicinity of the longest bar (bottom) but the long wavelength peaks strongly suppressed at the shortest bar. (c) Field intensity spectrum measured at the shortest bar (blue) and longest bar (red). Again, we see that all four peaks are evident on the long bar, but only two are prominent for the short bar.

used a total-field scattered-field (TFSF) technique<sup>32,33</sup> to provide the plane wave source. The computational domain is surrounded by perfectly matched layer boundary conditions. For a two-dimensional structure, the capacitance, inductance, and resistance have units of F/m, H·m, and Ω·m, respectively. The choice of the structural parameters here corresponds a two-dimensional capacitance, inductance, and resistance values of  $C/a$ ,  $L/a$ , and  $R/a$ , respectively, where the values of  $C$ ,  $L$ , and  $R$  are provided in Table 1 and  $a = 30$  nm, if we use the analytic circuit model as provided above where gold is treated with a Drude model with  $\omega_p = 1.372 \times 10^{16}$  rad/sec and  $\gamma = 4.059 \times 10^{13}$  rad/sec.<sup>34</sup> We note, however, that such a simple analytic model only provides a qualitative description of the antenna behavior. The dielectric constants of gold used in the simulation<sup>22</sup> deviate somewhat from the Drude model. Moreover, it is known that to quantitatively describe the antenna structure with a circuit model, a number of additional circuit elements need to be incorporated. Here, we use the simple circuit model to illustrate the main physics of the structure.

In Figure 5b, we plot the field intensity as a function of wavelength along a line that is located 2 nm away from the straight edge of the device, as illustrated in Figure 5a. Consistent with the prediction from the circuit theory, at the smallest resonant wavelengths, we observe intensity enhancements at the end of all the metal bars, whereas at largest resonant wavelengths, the enhancement is prominent only near the longest bars. In Figure 5c, we plot the spectra of the intensity enhancement next to the shortest and the longest bar on the same plot and confirm that all four resonances are present on the long bar (red), whereas only the lowest wavelength peaks are observed on the short bar (blue), again in agreement with the prediction from the circuit theory.

In Figure 5, we have used a relatively simple antenna structure to illustrate the underlying physics. Further enhancement of the field intensity can be accomplished by introducing a second array of dipole antennas and by placing a pair of sharp tips on the longest bars of our physical structure to utilize the lightning-rod effect<sup>35</sup> to increase the field intensity at this point. The resulting structure, as shown originally in Figure 1, enables multiresonant field intensity enhancement between the two tips that is 10–100 times higher than that from the structure in Figure 5.

The physics as illustrated above can also be implemented in three-dimensional structures. In Figure 6, we consider two

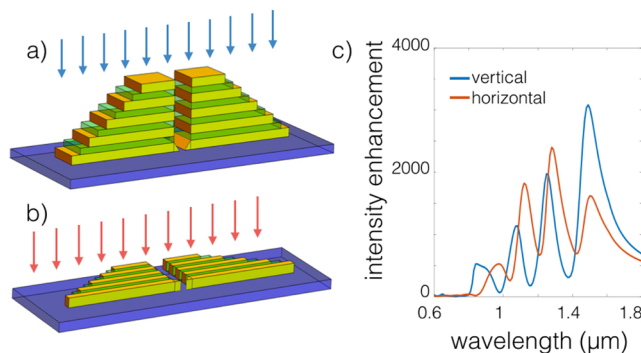


**Figure 6.** Simulation (three-dimensional) results for two configurations: (a) vertical and (b) horizontal. Both configurations have an incoming wave with polarization along the horizontal direction. (c) Field-intensity enhancement as a function of wavelength for the vertical (blue) and horizontal (red) configurations. Substrates and gaps are modeled as SiO<sub>2</sub>, with optical properties taken from tabulated data.<sup>36</sup> As in the two-dimensional case, the metallic sections are modeled as gold using tabulated optical properties. Bar lengths are {180,160,140,120,100} nm. Metal and gap thicknesses are 20 and 15 nm, respectively. Metal length in the perpendicular direction is 30 nm. The four resonant peaks are expressed in each configuration. Presence of a substrate in the horizontal configuration causes red-shifting of the short resonance wavelengths.

antenna configurations, each of which consists of an array of pairs of metal-wires with varying lengths, with silicon oxide regions between the nearest neighboring pairs of metal wires and with two tip regions attached to the longest metal wires, forming the hot spot in between. Both antennae are placed on top of a silicon oxide substrate, either in a vertical (Figure 6a) or a horizontal (Figure 6b) orientation. Both configurations display multiresonant field enhancements at the hot spot as long as the light polarization is parallel to the metal bars. The horizontal orientation (Figure 6b), where all gap regions are in the immediate vicinity of the oxide substrate, have resonant

wavelengths that are red-shifted as compared to the vertical orientation shown in Figure 6a. Simulations show that the fields are relatively constant along the thickness direction of the structures perpendicular to the incident polarization. Therefore, the physics of these three-dimensional structures are quite similar to the simpler two-dimensional structures considered earlier. Both configurations should be implementable experimentally. For the vertical structure, metal–oxide layers may be deposited on a substrate and etched to form a pyramid structure with a central gap. For the horizontal structure, a metallic layer may be deposited on a substrate, and the gaps may be fabricated by ion milling.

The structures presented in this paper trap light with individual MIM gap plasmonic resonances, as shown, for example, in Figure 1b. Therefore, the frequencies of the resonances are easily controlled. By individually controlling lengths and thicknesses of the metal bars, as well as the material and width of the gap regions, one may individually tune the resonance wavelengths of the device. The resonance wavelength of a single gap is directly proportional to the length of the smaller of the two enclosing metal bars, making this a straightforward parameter for tuning. To have isolated resonances in individual gaps, the thickness of the metal bars must be sufficiently large (>15 nm) to reduce coupling between the modes of adjacent gaps. When the gap thickness is decreased, the propagation constant of the guided mode is increased and the resonance wavelength subsequently increased.<sup>37</sup> Therefore, assuming minimal coupling between gaps, the resonance wavelength of a gap can be determined from the effective index of the asymmetric bound mode of the MIM waveguide, ( $n_{\text{eff}}$ ), the order ( $m$ ) of the resonance, and the length of the shortest bar ( $L$ ) in the following way:

$$\lambda_0^{(m)} \approx 4\pi \frac{n_{\text{eff}}L}{(2\pi m - \phi_r)}$$

where  $\phi_r$  is the reflection phase at the end of the MIM waveguide.<sup>38</sup> We focused on  $m = 1$  in this paper as it gives the highest field enhancement and has resonances that occur in the visible–NIR wavelengths for our geometric parameters.

In summary, we have introduced a theoretical framework, based on a simple circuit model, for the systematic design of metallic nanoantenna structures capable of multiresonant field enhancement at a single location. We realize the circuit model in a metallic nanostructure consisting of multiple metal wires with varying lengths and numerically demonstrate multiresonance field enhancement at a single hot spot between two tips attached to the wires of largest length. Our work should be important for designing antenna structures for a number of sensing and photodetection applications. For SERS and molecular sensing experiments, for example, these multiresonant nanostructures will enable simultaneous enhancement of signals from several energy transitions, which may further enhance the efficiency of these processes. In general, our work identifies a mechanism through which one can flexibly design multiresonant spectra for optical antennas, which can benefit applications such as sensing and photodetection. Our finding also shows that the plasmonic circuit model provides a useful framework with which to formulate design strategies for plasmonic nanoantenna structures.

## AUTHOR INFORMATION

### Corresponding Author

\*E-mail: shanhui@stanford.edu.

### Notes

The authors declare no competing financial interest.

## ACKNOWLEDGMENTS

The authors thank Y. Shi for helpful discussions on developing the circuit model. This work was supported in part by an AFOSR-MURI program (grant no. FA9550-12-1-0024).

## REFERENCES

- (1) Adato, R.; Yanik, A. A.; Amsden, J. J.; Kaplan, D. L.; Omenetto, F. G.; Hong, M. K.; Erramilli, S.; Altug, H. Ultra-Sensitive Vibrational Spectroscopy of Protein Monolayers with Plasmonic Nanoantenna Arrays. *Proc. Natl. Acad. Sci. U. S. A.* **2009**, *106* (46), 19227–19232.
- (2) Schuller, J. A.; Barnard, E. S.; Cai, W.; Jun, Y. C.; White, J. S.; Brongersma, M. L. Plasmonics for Extreme Light Concentration and Manipulation. *Nat. Mater.* **2010**, *9* (3), 193–204.
- (3) Crozier, K. B.; Sundaramurthy, A.; Kino, G. S.; Quate, C. F. Optical Antennas: Resonators for Local Field Enhancement. *J. Appl. Phys.* **2003**, *94* (7), 4632–4642.
- (4) Kinkhabwala, A.; Yu, Z.; Fan, S.; Avlasevich, Y.; Müllen, K.; Moerner, W. E. Large Single-Molecule Fluorescence Enhancements Produced by a Bowtie Nanoantenna. *Nat. Photonics* **2009**, *3* (11), 654–657.
- (5) Tam, F.; Goodrich, G. P.; Johnson, B. R.; Halas, N. J. Plasmonic Enhancement of Molecular Fluorescence. *Nano Lett.* **2007**, *7* (2), 496–501.
- (6) Talley, C. E.; Jackson, J. B.; Oubre, C.; Grady, N. K.; Hollars, C. W.; Lane, S. M.; Huser, T. R.; Nordlander, P.; Halas, N. J. Surface-Enhanced Raman Scattering from Individual Au Nanoparticles and Nanoparticle Dimer Substrates. *Nano Lett.* **2005**, *5* (8), 1569–1574.
- (7) Kneipp, K.; Wang, Y.; Kneipp, H.; Perelman, L. T.; Itzkan, I.; Dasari, R. R.; Feld, M. S. Single Molecule Detection Using Surface-Enhanced Raman Scattering (SERS). *Phys. Rev. Lett.* **1997**, *78* (9), 1667.
- (8) Vo-Dinh, T.; Wang, H. N.; Scaffidi, J. Plasmonic Nanoprobes for SERS Biosensing and Bioimaging. *J. Biophotonics*. **2010**, *3* (1–2), 89–102.
- (9) Novotny, L.; Van Hulst, N. Antennas for Light. *Nat. Photonics* **2011**, *5* (2), 83–90.
- (10) Bharadwaj, P.; Deutsch, B.; Novotny, L. Optical Antennas. *Adv. Opt. Photonics* **2009**, *1* (3), 438–483.
- (11) Mühlischlegel, P.; Eisler, H. J.; Martin, O. J. F.; Hecht, B.; Pohl, D. W. Resonant Optical Antennas. *Science* **2005**, *308* (5728), 1607–1609.
- (12) Novotny, L. Effective Wavelength Scaling for Optical Antennas. *Phys. Rev. Lett.* **2007**, *98* (26), 266802.
- (13) Fromm, D. P.; Sundaramurthy, A.; Schuck, P. J.; Kino, G.; Moerner, W. E. Gap-Dependent Optical Coupling of Single “Bowtie” Nanoantennas Resonant in the Visible. *Nano Lett.* **2004**, *4* (5), 957–961.
- (14) Grober, R. D.; Schoelkopf, R. J., III; Prober, D. E. High Efficiency Near-Field Electromagnetic Probe Having a Bowtie Antenna Structure. U.S. Patent 5,696,372, Dec 9, 1997.
- (15) Alda, J.; Rico-García, J. M.; López-Alonso, J. M.; Boreman, G. Optical Antennas for Nano-Photonic Applications. *Nanotechnology* **2005**, *16* (5), S230.
- (16) Sederberg, S.; Elezzabi, A. Y. Sierpiński Fractal Plasmonic Antenna: A Fractal Abstraction of the Plasmonic Bowtie Antenna. *Opt. Express* **2011**, *19* (11), 10456–10461.
- (17) Gottheim, S.; Zhang, H.; Govorov, A. O.; Halas, N. J. Fractal Nanoparticle Plasmonics: The Cayley Tree. *ACS Nano* **2015**, *9* (3), 3284–3292.

- (18) Volpe, G.; Volpe, G.; Quidant, R. Fractal Plasmonics: Subdiffraction Focusing and Broadband Spectral Response by a Sierpinski Nanocarpenter. *Opt. Express* **2011**, *19* (4), 3612–3618.
- (19) Navarro-Cía, M.; Maier, S. A. Broad-Band Near-Infrared Plasmonic Nanoantennas for Higher Harmonic Generation. *ACS Nano* **2012**, *6* (4), 3537.
- (20) Aouani, H.; Rahmani, M.; Šípová, H.; Torres, V.; Hegnerová, K.; Beruete, M.; Homola, J.; Hong, M.; Navarro-Cía, M.; Maier, S. A. Plasmonic Nanoantennas for Multispectral Surface-Enhanced Spectroscopies. *J. Phys. Chem. C* **2013**, *117* (36), 18620.
- (21) Aouani, H.; Šípová, H.; Rahmani, M.; Navarro-Cía, M.; Hegnerová, K.; Homola, J.; Hong, M.; Maier, S. A. Ultrasensitive Broadband Probing of Molecular Vibrational Modes with Multi-frequency Optical Antennas. *ACS Nano* **2013**, *7* (1), 669.
- (22) Johnson, P. B.; Christy, R. W. Optical Constant of Transition Metals: Ti, V, Cr, Mn, Fe, Co, Ni, and Pd. *Phys. Rev.* **1974**, *9*, 5056–70.
- (23) Kocabas, S. E.; Veronis, G.; Miller, D. A.; Fan, S. Transmission Line and Equivalent Circuit Models for Plasmonic Waveguide Components. *IEEE J. Sel. Top. Quantum Electron.* **2008**, *14* (6), 1462–1472.
- (24) Benz, F.; De Nijs, B.; Tserkezis, C.; Chikkaraddy, R.; Sigle, D. O.; Pukenas, L.; Evans, S. D.; Aizpurua, J.; Baumberg, J. J. Generalized Circuit Model for Coupled Plasmonic Systems. *Opt. Express* **2015**, *23* (26), 33255–33269.
- (25) Engheta, N.; Salandrino, A.; Alù, A. Circuit Elements at Optical Frequencies: Nanoinductors, Nanocapacitors, and Nanoresistors. *Phys. Rev. Lett.* **2005**, *95* (9), 095504.
- (26) Engheta, N. Circuits with Light at Nanoscales: Optical Nanocircuits Inspired by Metamaterials. *Science* **2007**, *317* (5845), 1698–1702.
- (27) Zhu, D.; Bosman, M.; Yang, J. K. A Circuit Model for Plasmonic Resonators. *Opt. Express* **2014**, *22* (8), 9809–9819.
- (28) Simovski, C. Circuit Model of Plasmon-Enhanced Fluorescence. *Photonics*. **2015**, *2* (2), 568–593.
- (29) Staffaroni, M.; Conway, J.; Vedantam, S.; Tang, J.; Yablonovitch, E. Circuit Analysis in Metal-Optics. *Phot. Nano. Fundam. Appl.* **2012**, *10* (1), 166–176.
- (30) Shin, W.; Fan, S. Choice of the Perfectly Matched Layer Boundary Condition for Frequency-Domain Maxwell's Equations Solvers. *J. Comput. Phys.* **2012**, *231* (8), 3406–3431.
- (31) Veronis, G.; Dutton, R. W.; Fan, S. A New Method for Sensitivity Analysis of Photonic Crystal Devices. *Opt. Lett.* **2004**, *29*, 2288–2290.
- (32) Taflov, A.; Hagness, S. C. *Computational Electrodynamics*; Artech House Publishers: London, 2005.
- (33) Rumpf, R. C. Simple Implementation of the Arbitrarily Shaped Total-Field/Scattered-Field Regions in Finite-Difference Frequency-Domain. *Progress in Electromagnetics Research B* **2012**, *36*, 221–248.
- (34) Ordal, M. A.; Bell, R. J.; Alexander, R. W.; Long, L. L.; Querry, M. R. Optical Properties of Fourteen Metals in the Infrared and Far Infrared: Al, Co, Cu, Au, Fe, Pb, Mo, Ni, Pd, Pt, Ag, Ti, V, and W. *Appl. Opt.* **1985**, *24* (24), 4493–4499.
- (35) Liao, P. F.; Wokaun, A. Lightning Rod Effect in Surface Enhanced Raman Scattering. *J. Chem. Phys.* **1982**, *76* (1), 751–752.
- (36) Palik, E. D. *Handbook of Optical Constants of Solids*; Academic: Cleveland, OH, 1985.
- (37) Veronis, G.; Fan, S. Theoretical Investigation of Compact Couplers Between Dielectric Slab Waveguides and Two-Dimensional Metal-Dielectric-Metal Plasmonic waveguides. *J. Lightwave Technol.* **2007**, *25*, 2511.
- (38) Barnard, E. S.; White, J. S.; Chandran, A.; Brongersma, M. L. Spectral Properties of Plasmonic Resonator Antennas. *Opt. Express* **2008**, *16* (21), 16529–16537.